Activated porous carbon supported Pd and ZnO nanocatalysts for trace sensing of carbaryl pesticide in water and food products

Rihem Jemai,[a] Mohamed Amine Djebbi,*[ab] Navid Hussain,[c] Bingquan Yang,[c] Michael Hirtz,[c] Vanessa Trouillet,[d] Hafsia Ben Rhaiem[a] and Abdesslem Ben Haj Amara[a]

Nanomaterials-based sensors are direly needed as a monitoring tool for the credible and accurate determination of pesticides in water and food samples. Herein, electrocatalysts of Pd and ZnO nanoparticles (NPs) supported on a highly porous framework of activated carbons (APC) were prepared for efficient electrochemical detection of carbaryl trace. First, activated potato starch was used as a pyrolysis precursor to obtain APC. The ZnO NPs were then grown on the APC substrate by sol gel/impregnation methods, followed by *in situ* reduction of Pd NPs. The as-prepared nanocomposite of Pd/ZnO/APC was morphologically and structurally confirmed by systematic physicochemical analysis. As-fabricated Pd/ZnO/APC nanocomposites were later evaluated for the efficient sensing of carbaryl by modifying a glassy carbon electrode (GCE). Cyclic voltammetry analysis revealed the unique oxidative sensing ability of Pd/ZnO/APC for carbaryl at 0.62 V with a low ΔE (80 mV) as compared to that of bare GCE. Based on the notable sensing ability of Pd/ZnO/APC, a reliable and sensitive electrochemical method was anticipated for the quantitative and qualitative determination of carbaryl. Meanwhile, experimental parameters, including electrolyte environment and electrodeposition conditions, were carefully refined to achieve maximum sensitivity and low detection limits. Under optimized conditions, the electrochemical sensing of carbaryl was realized with an LOD of 0.01 μM and a detection range of 0.01 5.0 μM. Moreover, the sensing electrode exhibited excellent selectivity, good reproducibility, and long-term stability, which qualified the sensor to analyze real samples, where it also showed satisfactory performance.

1. Introduction

Worldwide pesticide usage in agriculture has raised serious public concern regarding health, environment, and quality of foodstuff.[1,2] Most known pesticides are found in the agricultural sector, where water is used to irrigate crops, and can subsequently enter the human body through the food chain.[3] Pesticide residues impart serious hazards to human and non-target organisms and compromise the sustainability of the environment.[4] Among a large number of pesticides, carbaryl is the most widely used insecticide that shows a broad spectrum of activity and application. Carbaryl is the common name for the chemical, carbamic acid derivative 1-naphthyl *N*-methylcarbamate, which belongs to the carbamate pesticides class.[5,6] Although carbaryl pesticides are beneficial for crop production, the World Health Organization (WHO) has classified them as persistent pesticides due to their long-term contamination of groundwater, soil, and food,[7] which thereby represents a serious threat to human health. In particular, carbamate pesticides, being neurotoxins, can inhibit acetylcholinesterase action even at extremely low concentrations,[8–10] which produces severe and fatal physiological consequences to human health and life. Hence, precise tracking of these chemical residues in agricultural products and the environment is of utmost importance.

Existing methods available for the determination of trace levels of carbaryl include chromatographic and spectroscopic

---

[a] *Laboratory of Resources, Materials & Ecosystem (RME), University of Carthage, Faculty of Sciences of Bizerte, Zarzouna, 7021, Tunisia*

[b] *INRAE, UR RiverLy, Centre de Lyon Villeurbanne, 5 rue de la Doua CS 20244, Villeurbanne, 69625, France. E mail: med djebbi@hotmail.fr, mohammed amine.djebbi@inrae.fr; Tel: +216 27 380 672*

[c] *Institute of Nanotechnology (INT) and Karlsruhe Nano Micro Facility (KNMFi), Karlsruhe Institute of Technology (KIT), Hermann von Helmholtz Platz 1, 76344 Eggenstein Leopoldshafen, Germany*

[d] *Institute for Applied Materials (IAM ESS) and Karlsruhe Nano Micro Facility (KNMFi), Karlsruhe Institute of Technology (KIT), Hermann von Helmholtz Platz 1, 76344 Eggenstein Leopoldshafen, Germany*

techniques, such as gas chromatography (GC),[11,12] high-performance liquid chromatography (HPLC),[11] mass spectrometry (MS),[12] surface-enhanced Raman scattering (SERS),[13,14] UV-visible spectroscopy,[15] fluorescence,[16] and chemiluminescence,[17] *etc.* Despite the high sensitivity of these tools, they are not readily adapted for on-site monitoring due to their complexity, costs, and the requirement for highly-qualified operators. In addition, the polarity and thermal instability of carbaryl make its sensitive and accurate detection difficult. García de Llasera and Bernal-González[18] have reported that it is even difficult to detect carbamates using relatively modern techniques, such as liquid chromatography (LC) with post-column fluorescence detection or LC-diode array ultraviolet (UV) detection. Recently, standard immunoassays (*i.e.* ELISA, EIA, FPIA, *etc.*)[19,20] have become established techniques to detect carbamate pesticides, but such immunochemical methods are time-consuming and expensive; they may not always be sufficiently sensitive and can only be performed in centralized laboratories. Therefore, novel bioanalytical methodologies that are based on nanostructured electrochemical sensors[1,5,10,21–25] for the detection of carbaryl pesticides fulfill the requirements and have the potential to complement time- and labor-consuming luxurious analyzers currently used in modern laboratories. Applying electrochemical methods promises rapid results, accuracy, versatility, ease of use, and competitive costs.[23,26,27]

So far, numerous electrochemical sensors for carbaryl have been reported with various nanostructure-modified electrodes. Most of the carbaryl sensors were enzyme-based biosensors,[1,5,26,28–32] where acetylcholinesterase (AChE) enzymes were chosen as the biorecognition elements. Like most carbamate pesticides, carbaryl functions by inhibiting AChE, thus, it can bind reversibly to AChE. Despite the popularity of enzymatic sensors, considering enzyme specificity towards a certain species, the application of enzymatic systems remains limited. In addition, due to the intrinsic nature of enzymes, they require special care regarding pH, temperature, applied potential, storage, and may present loss of activity as well as low stability.[24,26,33] Given these drawbacks, non-enzymatic sensors based on nanomaterials are preferred due to their versatility, reliability, and precision. The feedback hitherto on non-enzymatic sensors, particularly those exploiting nanomaterials, has led to the deployment of a variety of functional electrode materials[22–25,34] since the sensitivity of an electrochemical sensor is influenced by its specific surface area and electrical conductivity. As reported in the previous works,[5,10,23,35,36] the applicability of bare glassy carbon electrode (GCE) for routine analysis of carbaryl in water and food samples has been extensively envisaged and discussed thanks to its relatively low cost, extreme resistance, chemical inertness, specific surface orientation, and wide potential window.[37,38] However, it cannot be ignored that the limited surface-to-volume ratio and electron transfer rate, as well as the overpotential of GCEs, hinders their wide application. Therefore, the study of effective catalysts to modify bare electrodes is essential to designing and constructing high-performance chemical sensors.

Recently, a variety of surficial electrocatalyst nanostructures have been reported and investigated by researchers for the development of electrochemical sensors. Among these, semiconducting zinc oxide (ZnO) nanoparticles have become very popular over the past few years for application in sensor sciences because of their promising chemical, electrical, and thermal stabilities; low cost; lack of toxicity; and excellent electro-catalytic activity as compared to other metal oxides.[39–42] Regrettably, the sensing aptitude of ZnO NPs is restricted by the fast recombination of the generated electron–hole pairs, which reduces their capability for direct electron transfer.[43] Instead, coupling nanostructured ZnO with co-catalysts is the key to liberating the captured-(stored)-electrons and accelerating the electron transfer rate at interfaces. In particular, noble metal nanoparticles, such as palladium (Pd), have been reported to greatly improve the electrochemical properties of ZnO.[44] Pd NPs can act as an inhibitor of charge recombination, which facilitates charge mobility and transportation, thereby creating more active sites for the catalytic reaction. In addition, Pd NPs have emerged as exciting nanomaterials due to their unique physical and chemical properties resulting from their high surface-to-volume ratio and nanoscale size. Furthermore, Pd-based ZnO nanocomposite has also been found to be a worthy electrocatalyst for electrochemical sensing applications and the detection of trace contaminants in water and food products.[42,44–46] However, despite the advantageous attributes of Pd and ZnO NPs, their immobilization on a solid support is often required to prevent aggregation and facilitate the application of the electrocatalyst.

Activated porous carbon (APC) has attracted our attention to building up a sensitive and reliable sensor. APC features unique properties, such as excellent chemical stability, huge surface area, high porosity, electrical conductivity, and the presence of oxygen functionalities on the surface. Therefore, it offers more advantages in terms of stabilizing metal and metal oxide NPs and rapid electron transfer, thereby having extensive application in electrochemical sensors.[47–50] The uniform dispersion of either ZnO or Pd NPs on APC, where APC acts as a support to anchor metallic NPs, has been widely reported.[47,48] Existing research indicates that the *in situ* formation of Pd and/or ZnO NPs on the porous carbon frameworks may remarkably enhance their catalytic activity and stability, while exposing the active sites to the interface completely, thereby greatly improving the sensing performance.[47,48] However, to the best of our knowledge, nanocomposites consisting of the three components, Pd, ZnO, and APC, have not yet been reported in the literature. Herein, the development of Pd/ZnO/APC nanocatalysts for the efficient electrochemical detection of trace levels of carbaryl pesticide has been described for the first time. The incorporation of Pd and ZnO NPs along with APC substrate produces a synergetic effect and rapid electron transport at regulated experimental conditions for the detection of carbaryl analytes. The Pd/ZnO/APC nanocomposite is characterized by X-ray diffraction (XRD), Fourier transform-infrared spectroscopy (FT-IR), X-ray photoelectron spectroscopy (XPS), transmission electron microscope (TEM), scanning electron microscopy (SEM), atomic force microscopy (AFM), and nitrogen adsorption/desorption isotherm. For fabrication of the sensing electrode, the Pd/ZnO/APC nanocatalyst dripped onto a GCE surface and a highly sensitive square wave voltammetry (SWV) technique has been anticipated to trace out residue level of carbaryl pesticides. The achieved linear range (LR) toward carbaryl detection was 0.01–5 μM, and the limit of detection (LOD) was 0.01 μM. The Pd/ZnO/APC/GCE exhibited excellent selectivity, high reproducibility, and good stability, which ensured the potential practical applicability of the sensing electrode on fresh water and food samples.

2. Experimental section

2.1. Chemicals and reagents

Starch powder from potato ($(C_6H_{10}O_5)_n$); zinc chloride ($ZnCl_2$, ≥98%); palladium(II) chloride ($PdCl_2$, ≥99.9%); sodium phosphate, dibasic, heptahydrate ($Na_2HPO_4 \cdot 7H_2O$, 98.0–102.0%); hydrazine hydrate ($NH_2NH_2 \cdot H_2O$, 98%); potassium ferrocyanide(II) trihydrate ($K_4Fe(CN)_6 \cdot 3H_2O$, 98.5–102.0%); potassium hexacyanoferrate(III) ($K_3Fe(CN)_6$, ≥99.9%); sodium hydroxide (NaOH, ≥98%); hydrochloric acid (HCl, 37%); phosphoric acid (H_3PO_4, 99.99%); potassium chloride (KCl, 99.0–100.5%); sodium chloride (NaCl, ≥99.0%); calcium chloride ($CaCl_2$, ≥97%); magnesium chloride hexahydrate ($MgCl_2 \cdot 6H_2O$, 99.0–102.0%); cadmium(II) nitrate tetrahydrate ($Cd(NO_3)_2 \cdot 4H_2O$, 99%); ammonium nitrate (NH_4NO_3, ≥98%); L-ascorbic acid ($C_6H_8O_6$, 99%); acetonitrile (CH_3CN, 99.8%); and ethanol (CH_3CH_2OH, 96.0–97.2%) were analytical grade. They were purchased from Sigma-Aldrich and used without further purification. Carbaryl, atrazine, and bromoxynil pesticides were obtained from Supelco Analytical (USA). The supporting electrolyte used in these experiments was phosphate buffer solution (PBS, 0.1 M, pH 4.5). All solutions were prepared in distilled water. The pH of the buffer solution was adjusted using a pH meter with 0.1 M NaOH and 0.1 M HCl solutions. Drinking water and tomato juice were used as is to detect spiked carbaryl.

2.2. Synthesis of Pd/ZnO/APC nanocomposite

The carbonaceous materials were chemically activated using phosphoric acid and prepared by hydrothermal carbonization (Scheme 1). Briefly, a potato starch (PS) sample was thoroughly soaked in (1 M) H_3PO_4 for 30 min. The mixture was then dried at 100 °C and held at this temperature for 1 h. Subsequently, the dried and activated PS materials were carbonized for 2 h at 700 °C in the presence of N_2 gas in a tubular furnace. The pyrolyzed carbon material was then ground to produce fine powder denoted as APC.

ZnO/APC composite precursors were synthesized by the wet-chemical method (sol–gel/impregnation). Typically, 4.70 g zinc chloride was wholly dissolved in 50 mL of distilled water and stirred for 30 min to obtain solution A. Simultaneously, 3 g APC was gradually added to 50 mL of distilled water, stirred, and thoroughly sonicated for 30 min to obtain solution B. The mixture of solutions A and B was stirred for an additional 30 min until its pH value was adjusted to 9 by adding NaOH (0.5 M). A grey ZnO/APC gel was formed and allowed to age overnight. The mixture was then washed with distilled water, oven-dried at 100 °C, and finally, annealed in a N_2 furnace at 500 °C for 2 h. The sample so prepared was denoted as ZnO/APC. Later, Pd NPs were synthesized *in situ* onto the APC/ZnO composite. In brief, 60 mg $PdCl_2$ and 200 mg APC/ZnO were mixed and ground in a mortar with an agate pestle for 10 min, dissolved in 25 mL ethanol, and stirred at room temperature for 2 h. After that, the solution was vaporized at 80 °C for 4 h, washed thrice with ethanol, placed in a vacuum drying oven,

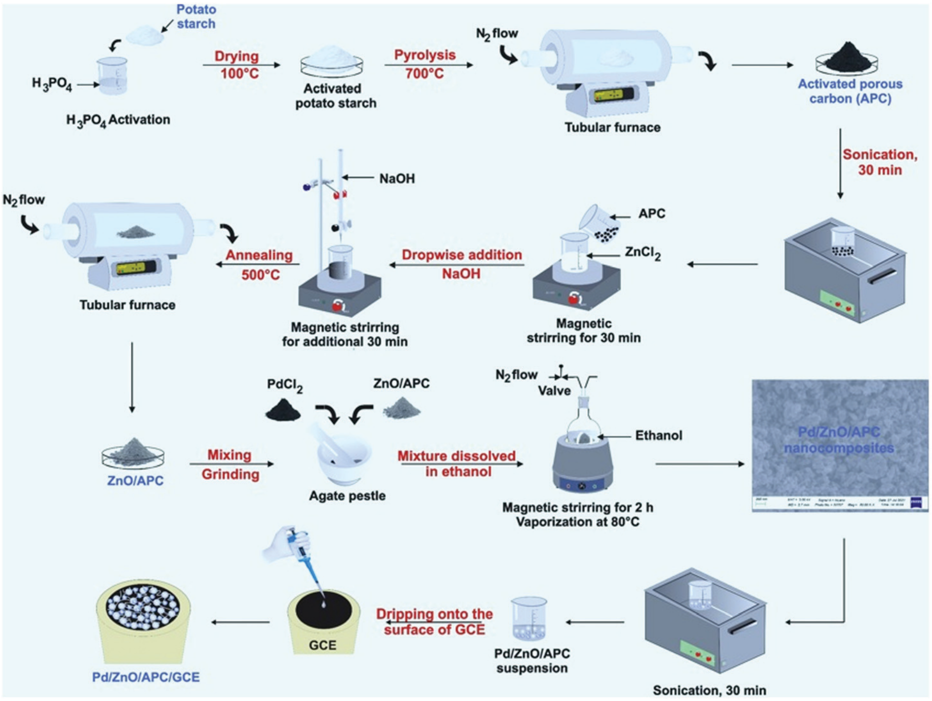

Scheme 1 Schematic illustration of the synthesis route for Pd/ZnO/APC nanocomposites and their application to the electrochemical sensor.

and dried at 100 °C overnight. The final product was labeled Pd/ZnO/APC nanocomposite.

2.3. Materials characterization

The crystalline structure and phase purity of the samples were investigated by X-ray diffraction (XRD) measurements on Bruker D8 Advance AXS diffractometer with CuKα radiation source (λ = 1.5406 Å) using the Bragg–Brentano diffraction method. The instrument was operated at 40 kV and 30 mA, and the data acquisition was performed with continuous scanning from 3.5 to 80° in steps of 0.01° and 76.59 s counting time per step. The functional groups of the samples were acquired on a Fourier-transform infrared (FT-IR) spectrometer (Nicolet 2000). Scans were collected in transmittance mode in the region of 4000–500 cm^{-1} with a spectral resolution of 1 cm^{-1} in ambient air by the KBr pellet method. The surface composition and chemical states were analyzed using a K-Alpha+ X-ray photoelectron spectrometer (ThermoFisher Scientific Instrument, UK), equipped with a monochromated AlKα X-ray source (400 μm spot size). The morphologies of the samples were visualized by transmission electron microscopy (TEM) and scanning electron microscopy (SEM). TEM images were taken using a Tecnai G2 FEI microscope, operating at an accelerating voltage of 200 kV, while SEM micrographs were obtained on a Zeiss Auriga microscope operated at an accelerating voltage of 5 kV. Atomic force microscopy (AFM) was also used to observe and analyze the microscopic surface morphology of the samples. All AFM images were recorded on a Dimension Icon system (Bruker, Germany) in tapping mode with silicon cantilevers from MikroMasch (HQ:NSC15/Al BS, nominal frequency 325 kHz, nominal force constant 40 N m^{-1}) and under atmospheric conditions. The textural features, including the specific surface area, total pore volume, and average pore diameter, were studied from nitrogen adsorption/desorption isotherms at 77 K using a physisorption apparatus (Micromeritics, ASAP 2020).

2.4. Preparation of modified electrodes

Before dealing with the electrode modification, the GCE first underwent a pre-treatment step to remove the impurity on its surface and improve its kinetics to achieve accurate and reproducible measurement results. Typically, the GCE was polished mechanically, with 0.5 nm alumina slurry on sandpaper and rinsed thoroughly with acetone, ethanol, and distilled water for 5 min. The electrode was then sonicated for 15 min in a mixture of ethanol and water (1 : 1, v/v) in an ultrasonic cleaning bath and finally dried at room temperature. Afterward, 6 μL of the prepared suspension (5 mg, in 2 mL distilled water) that had been previously sonicated for 30 min was dripped onto the pre-cleaned surface of the GCE (Scheme 1), dried at 60 °C for 30 min, and used for electrochemical experiments.

2.5. Electrochemical measurements

All the electrochemical measurements in this work were carried out at room temperature on an electrochemical analyzer (VoltaLab PGZ 100) workstation with the VoltaMaster 4 software for data acquisition and processing using a conventional three-electrode cell. A bare GCE or modified GCE served as a working electrode; a 0.5 mm platinum (Pt) wire as an auxiliary electrode, and a saturated calomel electrode (SCE) as a reference electrode. The electrochemical behavior of the modified electrode was examined by cyclic voltammetry (CV) and electrochemical impedance spectroscopy (EIS) in 10 mM $[\text{Fe(CN)}_6]^{3-/4-}$ redox probe solution. CV experiments were performed at a scan rate of 50 mV s^{-1} and a potential range from 600 mV to 600 mV. The EIS Nyquist plots were recorded over a frequency range from 100 mHz to 100 kHz with a 10 mV AC input and riding DC potential of 0.2 V. The electroanalytical sensitivity of the modified electrode toward carbaryl was evaluated using square wave voltammetry (SWV), in 0.1 M phosphate buffer (PBS, pH 4.5) in the potential range from 0.4 V to 1.0 V. The SWV parameters were optimized as regards frequency, pulse amplitude, and exposure time. The experimental conditions, such as the supporting electrolyte and electrolyte pH, were also explored and optimized. After each run of the experiment, a desorption scan was applied to the modified electrode in a blank solution to remove the residual pesticide.

3. Results and discussion

3.1. Physico-chemical characterization of materials

3.1.1. Structural characterization. The X-ray diffraction patterns (XRD) of APC, ZnO/APC, and Pd/ZnO/APC are shown in Fig. 1A. The bottom pattern shows the crystalline structure of the APC substrate. The wide diffraction peak at a 2θ value of 22.02° could be indexed to the (002) diffraction plane of hexagonal graphite carbon lattice.[48] The crystal information of ZnO grown on APC substrate is shown in the middle. The pattern exhibits eleven peaks at 2θ = 31.99, 34.68, 36.49, 47.79, 56.81, 63.10, 66.59, 68.37, 69.42, 73.03, and 77.32° belonging to the (100), (002), (101), (102), (110) (103), (220), (112), (201), (004), and (202) crystalline lattice planes of the hexagonal wurtzite phase of ZnO (JCPDS No. 36-1451), respectively.[51] However, the diffraction peak of porous carbon substrate was not found herein, suggesting that the crystalline phase of the carbon substrate had completely vanished. This can be explained by the fact that the carbon lattice likely lost its graphitized structure, while the ZnO NPs were homogeneously dispersed into the latter. Besides, the successful formation of the Pd NPs into the composite material could be investigated from the diffractogram of the Pd/ZnO/APC (top), where two additional peaks were observed at 2θ = 40.40 and 46.96°, corresponding to the characteristic reflection peaks, (111) and (200), of the face-centered cubic structure of metallic Pd (JCPDS No. 05-0681).[52] As in the ZnO/APC sample, the diffraction peak of the carbon substrate was not observed, while the shape, position, and strength of the ZnO diffraction peaks were similar, indicating the high thermal stability of ZnO in the nanocomposite. Further analysis based on the (100) and (111) peaks of ZnO and Pd NPs, respectively, with the Scherrer calculator using the PANalytical X'Pert HighScore Plus software

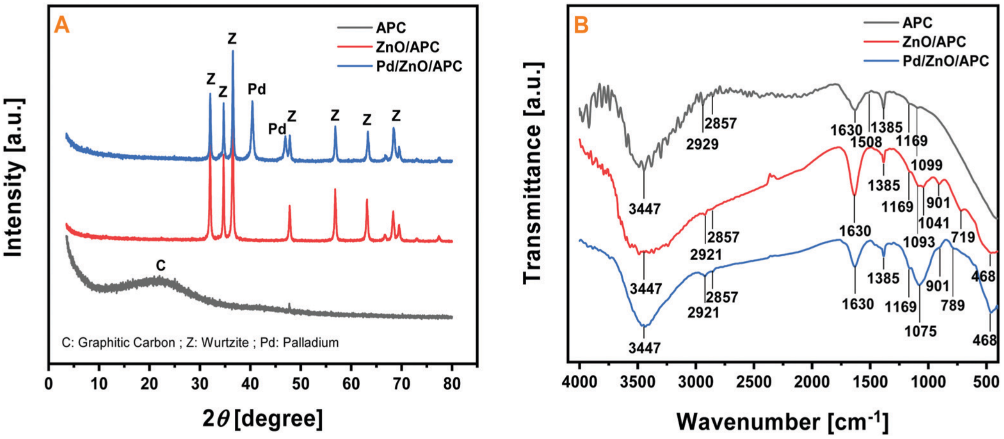

Fig. 1 (A) XRD patterns and (B) FT-IR spectra of the APC substrate, ZnO/APC, and Pd/ZnO/APC.

revealed an estimated average crystallite size of 3–5 nm for the Pd NPs and about 20 nm for ZnO in the Pd/ZnO/APC nanocomposite.

The chemical bonding characteristics of APC, ZnO/APC, and Pd/ZnO/APC were identified by Fourier transform infrared (FTIR) spectroscopy in the frequency range between 500 and 4000 cm^{-1}, and the spectra are presented in Fig. 1B. For the carbon substrate (top), five peaks identified at 1630, 1508, 1385, 1169, and 1099 cm^{-1} were involved in the region below 2000 cm^{-1}, corresponding to the intrinsic vibration of the carbon lattice.[53] The peaks at 1630 and 1099 cm^{-1} were assigned to the stretching of the C=O and C–O bonds in "pristine" carboxyl groups, respectively. The band around 1508 cm^{-1} could be attributed to the aromatic C=C ring stretching motion. The band that occurred at 1385 cm^{-1} suggested the presence of aliphatic carbon, and the absorption band at 1169 cm^{-1} was due to the C–C stretching. Furthermore, the wide peak observed at 3447 cm^{-1} confirmed the presence of oxygen in the form of OH derived from both H_3PO_4 activation and absorbed water, while those at 2929 and 2857 cm^{-1} could be assigned to asymmetric and symmetric C–H stretching vibrations. Upon loading ZnO on the porous carbon framework (middle), new vibration bands appeared at 1041, 901, 719, and 468 cm^{-1}.[54] They corresponded to asymmetrical and symmetrical Zn–O stretching vibrations. As compared to APC, the OH peak was broadened, indicating that the number of OH increased following the impregnation process, and the intensity peak of the C=O band was enhanced due to the overlap with the chloride anions derived from the unreacted precursor. In addition, the aliphatic stretching vibration of the APC (1385 cm^{-1}) was diminished, and the aromatic C=C ring stretching (1508 cm^{-1}) disappeared, implying that the presence of the ZnO onto the carbon lattice led to rearrangement toward a more disordered graphitic structure. This result is consistent with that deduced from XRD measurements. On the other hand, upon introducing the metal precursor (bottom), a notable shift in the C–O (1075 cm^{-1}) and Zn–O (789 cm^{-1}) vibrational bands was observed for the Pd/ZnO/APC, indicating its active involvement in the incorporation of Pd NPs onto the ZnO/APC matrix. Otherwise, there was no further change in the stated original positions of the main bands of the APC and the loading ZnO.

The surface chemical composition and chemical state in sensing materials APC, ZnO/APC, and Pd/ZnO/APC, were further investigated by XPS measurements as depicted in Fig. 2. APC was composed of carbon and oxygen, and C 1s showed a main asymmetric peak at 284.4 eV supporting the presence of sp^2-graphitized carbon,[55] accompanied by two weak peaks due to slight oxidation. Upon embedding ZnO onto the carbon substrate, Zn 2p with Zn $2p_{3/2}$ at 1021.8 eV could be detected (not shown here) as well as the Auger line Zn LMM. This latter was here essentially for the identification of the oxidation state and showed a maximum at ∼988 eV kinetic energy (Fig. 2), indicating the presence of ZnO.[56] The corresponding oxide peak in O 1s appeared at 530.5 eV and corresponded to O^{2-} of ZnO. Nevertheless, the ratio, Zn/O (530.5 eV), with a value of 1.4, together with the presence of an intensive O 1s peak at 531.9 eV, led to the assumption of the additional presence of an oxygen-deficient environment in the ZnO matrix and some hydroxide species. A further contribution at 533.0 eV was attributed to C=O, which was present in the carboxyl group and was detected in the C 1s at 289.0 eV. Contrary to what was observed for APC, the sp^2-graphitized carbon was not detected anymore, which confirmed the results obtained with XRD and FTIR surveys, whereby the porous carbon underwent degradation in the structural integrity of the graphitic carbon after uniform dispersion of the ZnO. Therefore, C 1s could be fitted with three peaks ascribed to the C–C or C–H (285.0 eV), C–O (286.7 eV), and O–C=O (289.0 eV) bonds. Lastly, Pd/ZnO/APC nanocomposite revealed that the Pd species embedded in the ZnO/APC matrix were successfully present in the metallic state Pd^0. As displayed in the high-resolution XPS spectrum of Pd, the Pd 3d doublet was deconvoluted in two asymmetric peaks at 334.5 (Pd $3d_{5/2}$) and 339.7 eV (Pd $3d_{3/2}$).[57] Likewise in the case of the ZnO/APC matrix, the ratio Zn/O (530.5 eV) remained at a value of 1.4. O 1s showed the same three components as C 1s.

3.1.2. Morphological characterization. The morphologies of the APC and its nanocomposite Pd/ZnO/APC were visualized by TEM at various magnifications as shown in Fig. 3. In Fig. 3A–C,

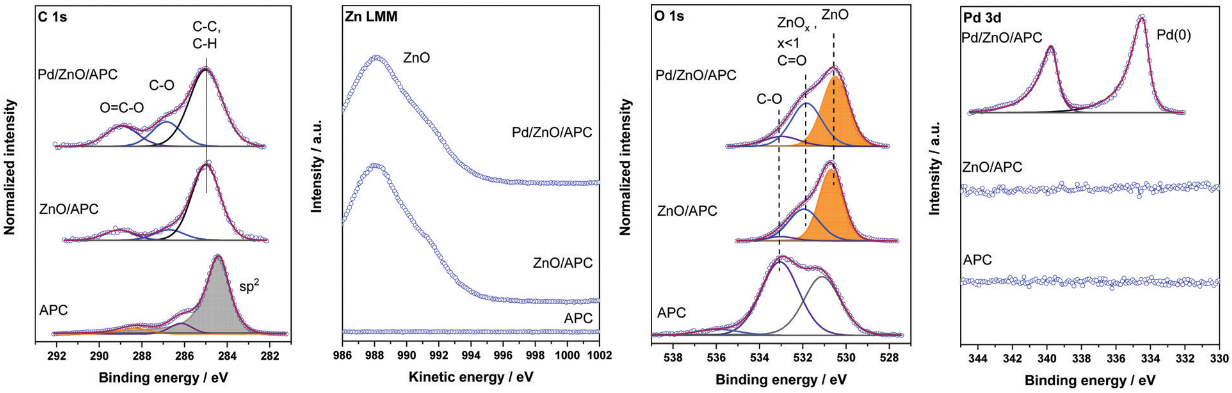

Fig. 2 C 1s, O 1s, and Pd 3d XPS spectra and Zn LMM Auger line of the APC substrate (bottom), ZnO/APC (middle), and Pd/ZnO/APC (top).

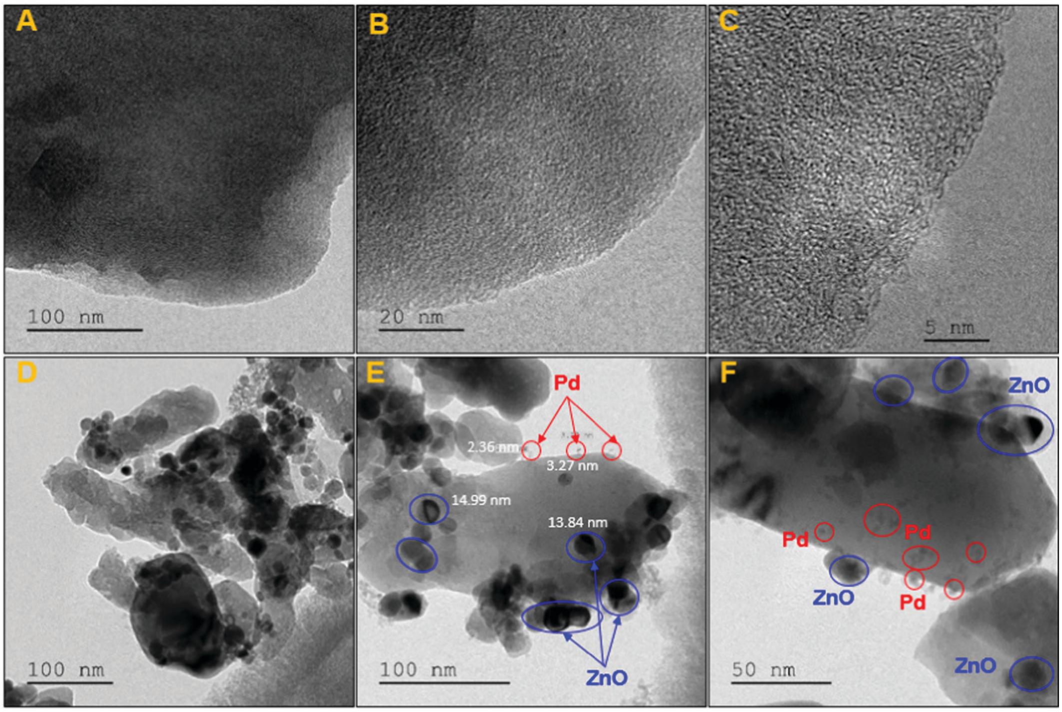

Fig. 3 TEM images of the APC substrate (A–C) and the Pd/ZnO/APC nanocomposite (D–F).

a disordered hierarchical porous structure with mesopores and micropores is discernable. The substantial quantities of white spots (Fig. 3B and C) in the corresponding micrographs resulted from the random stacking of sp^2-bonded carbon sheets and suggest that abundant micropores and mesopores co-exist in the activated carbon from potato starch. These pores are expected to produce sites where a sufficient number of Pd and ZnO nanoparticles can be anchored, thereby enhancing the electroactive surface area. However, Fig. 3D–F shows the embedded metal and metal oxide nanoparticles inside the carbon framework. It can be seen that large amounts of small and moderate nanoparticles were homogenously impregnated in the carbon template and had good dispersibility. ZnO crystal grains were present as dark and random nanoparticles ranging from spherical to elliptical shape with a size of around 20 nm (Fig. 3E and F), while the presence of Pd NPs was highlighted in grey with an average particle size of up to 5 nm (Fig. 3E and F). These results are thus consistent with those obtained using the computed XRD patterns.

Furthermore, SEM was also employed for the inspection of structural morphologies of the prepared samples, and the photographs are displayed in Fig. 4. From Fig. 4A–C, it can be observed that the pristine porous carbon exhibited a 3D smooth fracture surface of the carbon particles, suggesting a large specific surface area and abundant porous structure. But there were many wrinkles on the surface of the micro-sheets. These wrinkles on the surface of carbon particles were generated from evolution upon activation with H_3PO_4 and acted as

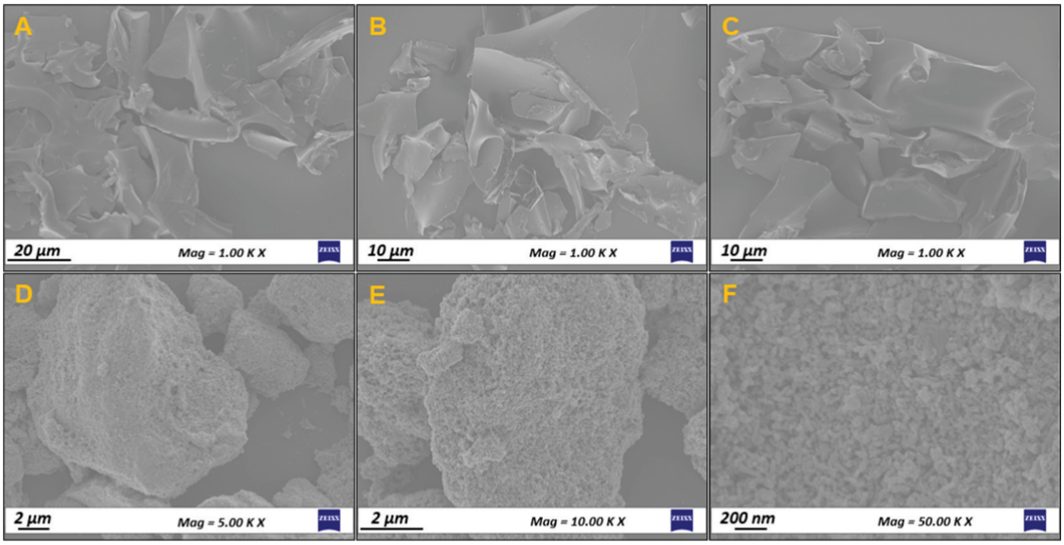

Fig. 4 SEM images of the APC substrate (A C) and the Pd/ZnO/APC nanocomposite (D F).

buffer pores to accommodate the volume change in the composite structure. Across the sol–gel synthesis of ZnO and the *in situ* reduction of Pd NPs, both metal and metal oxides were successfully loaded into the APC and dispersed well throughout the whole porous material (Fig. 4D and E). As compared to the APC matrix (Fig. 4F), a greater number of nanoparticles were present as aggregated clusters formed *in situ* on the porous carbon surface. Moreover, the Pd/ZnO/APC still had a typical 3D network structure, although ZnO, as well as Pd NPs, were uniformly distributed on the surface of the APC. Thus, the successful synthesis of the Pd/ZnO/APC nanocomposite was confirmed. Nevertheless, the 3D hierarchical structure constructed by porous carbon matrix, metal, and metal oxide nanoparticles would provide well-developed pore channels, serving as liquid flow pathways for the transport of carbaryl molecules to electroactive adsorption sites.

The size and morphology of Pd and ZnO NPs over the APC matrix were also investigated by recording 2-D (Fig. 5A and C) and 3-D (Fig. 5B and D) AFM images. The AFM analysis of APC materials (Fig. 5A and B) revealed the distribution of bigger "clumps". The height of these clumps reached 35 nm. In contrast to the surface of APC, the surface of the Pd/ZnO/APC (Fig. 5C and D) revealed the growth of highly oriented needles-like shapes corresponding to ZnO and Pd crystals. Their average size was estimated to be less than 20 nm according to the height profile of the AFM image. As per the AFM analysis, the average height of some Pd and ZnO NPs on the APC surface was ∼3.29 nm.

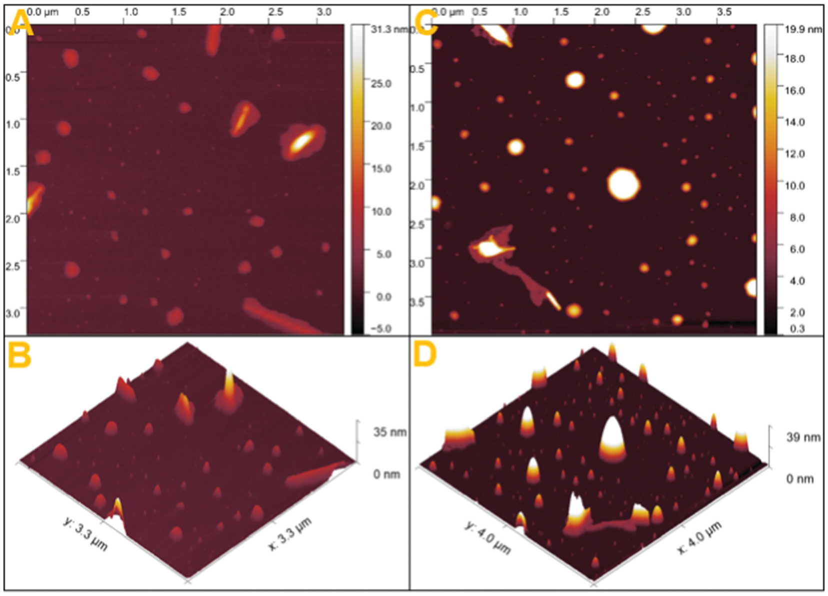

Fig. 5 AFM images of the APC substrate (A and B) and the Pd/ZnO/APC nanocomposite (C and D).

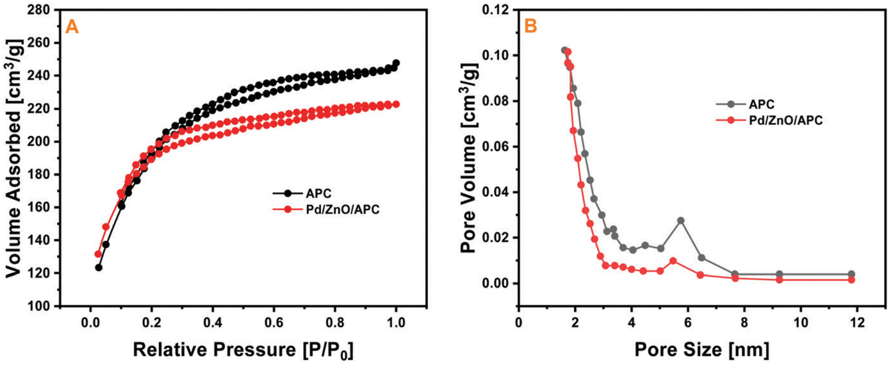

Fig. 6 Textural properties of the APC substrate and the Pd/ZnO/APC nanocomposite: (A) N_2 sorption isotherms and (B) the pore size distribution plots.

3.1.3. Textural characterization.

To gain insight into the structural evolution and confinement effects of the Pd and ZnO electrocatalysts into the carbon substrate, APC, the N_2 adsorption–desorption isotherms and the pore size distribution plots of the APC substrate and the Pd/ZnO/APC nanocomposite were recorded at 77 K. Fig. 6A shows the N_2 adsorption–desorption analysis. According to the IUPAC classification, a typical IV isotherm feature of mesoporous materials with a clear hysteresis in the relative P/P_0 range of 0.1–1.0 was obtained for both samples. The Brunauer–Emmett–Teller (BET) specific surface areas of the as-synthesized APC and Pd/ZnO/APC were calculated to be $\sim$790 and 685 $m^2\ g^{-1}$, respectively. The total pore volume and average pore diameter were estimated to be $\sim$1.55 $cm^3\ g^{-1}$ and 3.53 nm for APC and 1.26 $cm^3\ g^{-1}$ and 2.16 nm for Pd/ZnO/APC, respectively, as plotted by the Barrett–Joyner–Halenda (BJH) size distribution presented in Fig. 6B. Such a large specific surface area rendered the as-synthesized nanocomposite a promising candidate for pesticide uptake. However, the analysis also indicated the reduction in the microporous surface area and pore size of the carbon substrate upon loading Pd and ZnO nanoparticles on the surface of the latter. This can be explained by the blockage of the surface pore sites on the carbon substrate, which consequently, decreased the total surface area and pore size. These results are consistent with those obtained during structural characterization, where the carbon framework acted as a buffer layer to incorporate and control the aggregation of the nanoparticles. Nevertheless, the nanocomposite retained its porous structure that could be beneficial for a higher mass transfer process on the electrode surface.

3.2. Electrochemical characterization of the material

To investigate the electrocatalytic properties of the nanocomposite material, CV and EIS measurements were performed in a 0.1 M PBS buffer (pH 7.0) containing 10 mM $[\mathrm{Fe(CN)}_6]^{3-/4-}$ as a redox probe. CV experiments were mainly used to understand catalyst activity and kinetics.[58] Fig. 7A shows the cyclic voltammograms (scan rate of 50 mV s^{-1}) of the stepwise modification of the GCE: bare GCE, APC/GCE, ZnO/APC/GCE, and Pd/ZnO/APC/GCE. As expected, all the curves shown in Fig. 7A depict the standard redox peaks typical of reversible oxidation/reduction reactions of Fe^{2+} to Fe^{3+} and Fe^{3+} to Fe^{2+}. However, the observed oxidation (anodic) and reduction (cathodic) peak intensity, as well as peak-to-peak separation (ΔE), were different. Table 1 provides data on the electrochemical parameters of the CV curves for the different electrodes. The Pd/ZnO/APC/GCE displayed the highest anodic/cathodic peak currents and the smallest peak-to-peak separation value as compared to the

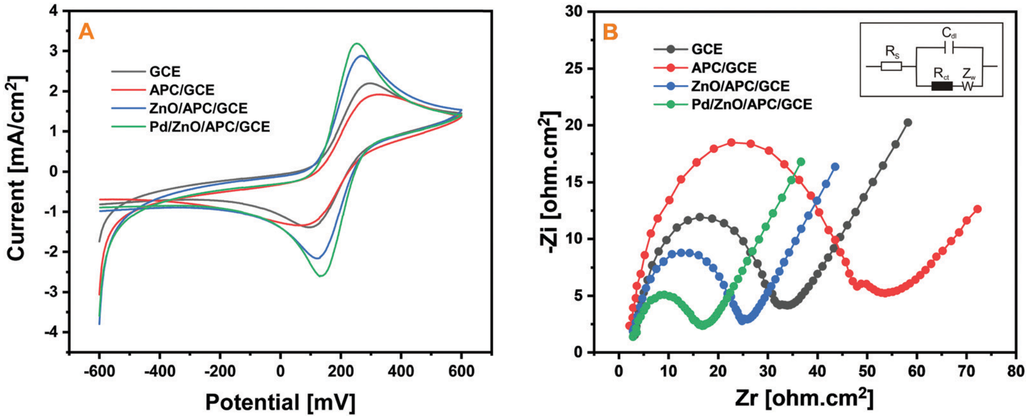

Fig. 7 (A) CV curves and (B) EIS Nyquist plots of GCE bare, APC/GCE, ZnO/APC/GCE, and Pd/ZnO/APC/GCE in 10 mM $[\mathrm{Fe(CN)}_6]^{3\ \ /4}$ redox probe solution.

other electrodes. The peak current decreased after the modification of the GCE with APC with an increase in the ΔE, which may be attributed to the low conductivity of the latter.[59] While coating the APC with ZnO NPs, peak currents were greatly increased (around 76% for I_{pa} and 63% for I_{pc} as compared to GCE bare) and electrode performance was improved, which can be explained by the enhanced conductivity issued by ZnO NPs due to their intrinsic electrocatalytic properties. This suggested that the metal oxide had facilitated electron transfer and enhanced the electroactive surface area of the electrode. Furthermore, upon the addition of Pd NPs, along with ZnO on the APC substrate, the Pd/ZnO/APC/GCE exhibited a further increase in the current (+1.10-fold and +1.44-fold than ZnO/APC/GCE and GCE bare, respectively) and a supplementary suppression in the ΔE (1.27-fold and   1.69-fold than ZnO/APC/GCE and GCE bare, respectively), indicating that the Pd/ZnO/APC nanocomposite allowed more electroactive sites for adsorption and better electrocatalytic ability as compared to the APC substrate alone and the ZnO/APC, which may offer better electrochemical reaction with the carbaryl molecules.

The enhancement in conductivity and electrocatalytic properties of the Pd/ZnO/APC nanocomposite was also confirmed using EIS experiments. EIS studies are commonly used to investigate electrode processes and quantify the charge-transfer kinetic properties of the electrocatalyst material.[60] The impedance spectra outlined herein were obtained in the frequency range from 100 mHz to 100 kHz at a constant applied potential of 200 mV; they are represented as Nyquist plots as displayed in Fig. 7B. The Nyquist diagrams of bare GCE, APC/GCE, ZnO/APC/GCE, and Pd/ZnO/APC/GCE all show a similar trend, which consists of a semicircle at high to medium frequencies and a straight tail line at low frequencies, corresponding to charge transfer and diffusion control,[61–63] respectively. The semicircle diameter in the Nyquist plot is a characteristic of the charge transfer resistance raised from the interface between the electrolyte and electrode; its value reflects the reaction kinetics of the redox probe. R_{ct} values listed in Table 1 were obtained by fitting the EIS data from the Randle's equivalent circuit that consisted of a cell resistance (R_S) in series with the parallel combination of the double-layer capacitance (C_{dl}) and a charge-transfer resistance (R_{ct}); here, Warburg impedance (Z_w) resulted from the diffusion of the $[Fe(CN)_6]^{3-/4-}$ species towards the electrode surface (inset of Fig. 7B). Calculated values followed this order: R_{ct}(APC/GCE) > R_{ct}(GCE) > R_{ct}(ZnO/APC/GCE) > R_{ct}(Pd/ZnO/APC/GCE). These computation results confirm those found previously by CV. The R_{ct} value of the GCE bare was about 30.0 ohm cm^2. After modification of the electrode by the carbon substrate, APC, the semicircle grew and the R_{ct} value increased to 48.15 ohm cm^2 suggesting that activated carbon suffers from low electrical conductivity with increasing porosity. The presence of micro-and mesopore delays the charge transfer, which limits accessibility to the electrode surface.[59] Once ZnO was added to the carbon support, the semicircle had strongly diminished and revealed an R_{ct} value of 23.09 ohm cm^2 because the conductivity of the electrode increased due to ZnO NPs, which facilitated electron transfer between the electrochemical probe redox and the electrode surface. Moreover, the presence of Pd NPs in the Pd/ZnO/APC nanocomposite led to further suppression in the semicircle with a low R_{ct} of 14.56 ohm cm^2. Pd NPs can indeed effectively increase the surface area to inhibit charge recombination, which eases the charge transfer and transportation processes, thereby creating more active sites for efficient catalytic reaction.[64,65]

3.3. Electrochemical behavior of carbaryl

To explore the electrochemical and kinetic profile of carbaryl, 50 μM of analyte was analyzed at bare GCE, APC/GCE, ZnO/APC/GCE, and Pd/ZnO/APC/GCE by cyclic voltammetry in 0.1 M PBS buffer (pH 4.5) with a scan rate of 50 mV s^{-1}. The results thus obtained for captured carbaryl are shown in Fig. 8A. On the GCE bare and APC/GCE, a weak and broad oxidation peak (E_{pa}, 0.70 and 0.76 V, respectively) was observed, corresponding to the oxidation of carbaryl. While on the ZnO/APC/GCE, a well-defined oxidation peak (E_{pa}, 0.66 V) of significantly-high current intensity was observed during CV analysis. Moreover, the peak potential shifted to less positive values, which were 0.04 and 0.1 V lower than those for GCE bare and APC/GCE, respectively, suggesting that the ZnO/APC/GCE had higher electrocatalytic activity towards the oxidation of carbaryl. This may be due to the availability of high catalytic active sites and the fast electron transfer rate exhibited by the ZnO NPs. Besides, once Pd NPs were incorporated, the Pd/ZnO/APC/GCE exhibited a further increase in the current intensity and a decrease in the oxidation potential with a well-resolved peak at 0.62 V. This improved performance was owed to the outstanding conductivity and high electrocatalytic properties of the Pd NPs. Nevertheless, it is noteworthy to point out that no reduction peak was found in the reverse scan over all the electrodes, indicating that the electrode reaction of carbaryl was an entirely irreversible process.

Table 1 Anodic and cathodic peaks were obtained from the CV curves and charge transfer resistances were determined using EIS Nyquist plots for GCE bare, APC/GCE, ZnO/APC/GCE, and Pd/ZnO/APC/GCE

Sample	I_{pa} (mA)	I_{pc} (mA)	E_{pa} (mV)	E_{pc} (mV)	ΔE (mV)	R_{ct} (ohm cm^2)
GCE	2.20	1.38	294.93	100.86	194.07	30.00
APC/GCE	1.92	1.32	317.92	81.71	236.21	48.15
ZnO/APC/GCE	2.87	2.16	268.44	122.25	146.19	23.09
Pd/ZnO/APC/GCE	3.18	2.60	252.48	137.89	114.59	14.56

I_{pa}: anodic current, I_{pc}: cathodic current, E_{pa}: anodic potential, E_{pc}: cathodic potential, ΔE: peak to peak separation potential, and R_{ct}: charge transfer resistance.

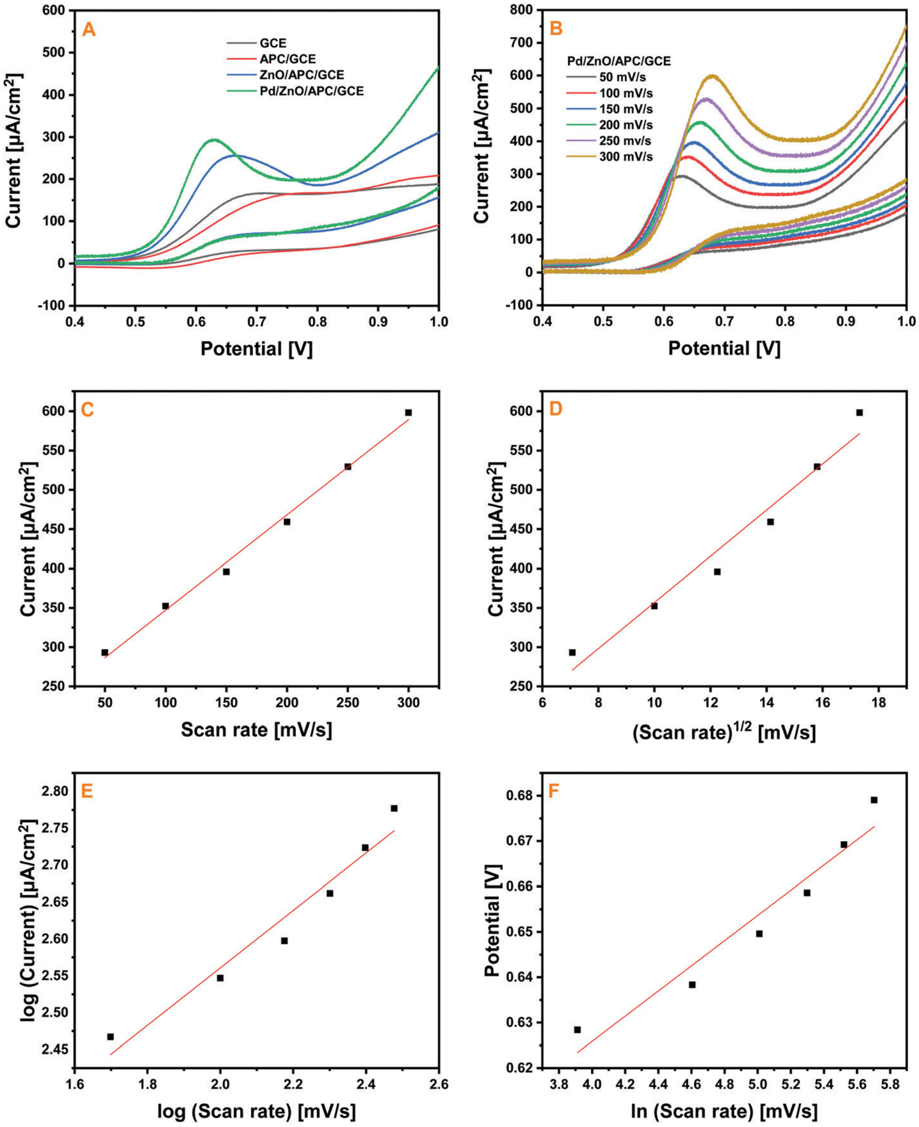

Fig. 8 (A) CV of 50 µM carbaryl at GCE bare, APC/GCE, ZnO/APC/GCE, and Pd/ZnO/APC/GCE in 0.1 M PBS (pH 4.5) with a scan rate of 50 mV s^{-1}; (B) CV of 50 µM carbaryl at Pd/ZnO/APC/GCE with different scan rates (50–300 mV s^{-1}); (C) plot of current *vs.* scan rate; (D) plot of current *vs.* square root of scan rate; (E) plot of log(current) *vs.* log(scan rate); (F) plot of potential *vs.* ln(scan rate).

To further study the electrocatalytic kinetic behavior of Pd/ZnO/APC/GCE toward carbaryl analytes, a supplementary CV analysis was performed with varying the scan rates from 50 to 300 mV s^{-1} under the conditions described above. Fig. 8B shows the CV responses of Pd/ZnO/APC/GCE with increasing scan rates of 50, 100, 150, 200, 250, and 300 mV s^{-1}. As can be seen in Fig. 8B, the corresponding voltammograms show similar trends, *i.e.*, a well-established oxidation peak of carbaryl in the anodic potential region and no corresponding reduction peak in the reverse scan. However, the current peaks show regular gradient slopes with rising scan rates, and the obtained plot (Fig. 8C) indicates a strong linear relationship between the scan rate and I_{pa} with a correlation coefficient (COD) of 0.9941. In addition to the increase in the peak currents, the irreversible oxidation peak potentials shifted to more positive values, which implies that the electrocatalytic oxidation of carbaryl over the surface of Pd/ZnO/APC/GCE was an irreversible adsorption-controlled process.[10]

Furthermore, the anodic current of carbaryl was plotted against the square root of the scan rate (Fig. 8D) to get better insight into whether the electrode reaction of carbaryl was adsorption and/or diffusion-controlled process. The plot showed a linear dependence between the peak current and the square root of the scan rate with a correlation coefficient of 0.9638, indicating that the electrocatalytic oxidation of carbaryl on the Pd/ZnO/APC/GCE surface underwent a diffusion-controlled reaction. A linear relationship was also acquired by plotting the logarithm of peak current *vs.* the logarithm of scan rate (Fig. 8E); the slope value of 0.38 in this plot indicated the ideal reaction condition for carbaryl to be the diffusion-controlled mechanism.[66,67] Based on the different plot studies, the carbaryl reaction on the Pd/ZnO/APC/GCE surface was attributed to a mixed effect involving adsorption and diffusion processes, as well as the adsorption of carbaryl species onto the electrode surface before diffusion for oxidation.

To further confirm the irreversible nature of the electrochemical processes of carbaryl, the relationship between the anodic potential and the logarithm of the scan rate could be expressed by the Laviron equation:[68]

$$E_{\text{pa}} = E_0 \quad \left(\frac{RT}{\alpha nF}\right) \ln\left(\frac{RTK_{\text{s}}}{\alpha nF}\right) + \left(\frac{RT}{\alpha nF}\right) \ln \nu \qquad (1)$$

where E_0 refers to formal redox potential, R is the universal gas constant, T is the absolute temperature, α gives the electron transfer coefficient, F indicates the Faraday constant, ν is the scan rate, and n is the electron transfer number. By plotting E_{pa} over $\ln \nu$ (Fig. 8F), the slope of the linear regression was found to be 0.04774. According to the Laviron equation, $\frac{RT}{\alpha nF}$ is equal to the slope; therefore, by substituting T = 298 K, R = 8.134 J K^{-1} mol^{-1}, F = 96 485, and α = 0.5 (for irreversible electrode reaction), n was estimated to be approximately 1.07. As the number of electrons in the carbaryl reaction was equal to the number of protons, it can be inferred that the electro-oxidation reaction of carbaryl at Pd/ZnO/APC/GCE involved a proton and electron each. Hence, the detection mechanism of carbaryl on Pd/ZnO/APC-modified GCE could be expressed as follows, which represents the prior oxidation of carbaryl to 1,4-naphthoquinone (Fig. 9).

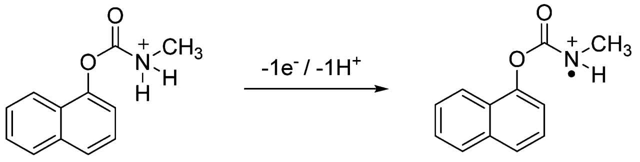

Fig. 9 The possible oxidation process of carbaryl occurring at the Pd/ZnO/APC/GCE surface.

3.4. Analytical performance for carbaryl detection

3.4.1. Optimization studies. To achieve good sensitivity for the quantitative analysis of carbaryl, various experimental conditions and parameters were optimized using square-wave voltammetry (SWV), such as the effect of the supporting electrolyte, the electrolyte pH, and the parameters associated with the SWV technique (frequency, pulse amplitude, and exposure time). The first parameter studied was the supporting electrolyte influence which is essential to electroanalytical assays.[69,70] Fig. 10A exhibits the current responses of Pd/ZnO/APC/GCE for 50 μM carbaryl in different supporting electrolytes, namely, 0.1 M hydrochloric acid (HCl), 0.1 M phosphate buffer (PBS, pH 4.5), 0.1 M acetate buffer (ABS, pH 5.0), and 3.0 M potassium chloride (KCl) solution. The maximum response was obtained with 0.1 M PBS as the electrolyte. Hence, phosphate buffer was chosen as the appropriate medium in the subsequent experiments. Another optimized parameter that strongly impacts the electrochemical behavior of electro-active organic compounds is the electrolyte pH.[60,71] The dependence of the electrocatalytic oxidation of carbaryl on pH was investigated in the pH range of 2.0 to 8.0 in the presence of 50 μM carbaryl in 0.1 M PBS buffer. The results obtained are shown in Fig. 10B, in which the current response was weak at pH 2 and then increased gradually to reach its peak at pH 4.5. Beyond this value (pH 4.5), the current intensity decreased to 8. This increase and decrease in the current response may result from the variation in the proton concentrations required to protonate the naphthol part of carbaryl. In an acidic medium, the naphthol part of carbaryl can be protonated, which influences the oxidation process and ultimately leads to a reduction in the peak current. While at higher pH values, 1-naphthol undergoes hydrolyzation to form a naphthoxide ion. In fact, hydroxide ion (OH^-) can extract a proton (H^+) of 1-naphthol, influencing the SWV currents.[36,72] As a result, pH 4.5 was chosen as the optimal value for further investigations.

On the other hand, to reduce capacitive and background currents, the measurement parameters associated with SWV were also optimized sequentially as depicted in Fig. 11. To examine these parameters, the Pd/ZnO/APC/GCE was immersed in 0.1 M PBS (pH 4.5) containing 50 μM carbaryl. Fig. 11A shows the effect of the variation of frequency on the current intensity in the range between 10 and 40 Hz, while maintaining the amplitude at 25 mV and extending the exposure time up to 90 s. It can be seen that the peak current increased rapidly up to a value of 25 Hz and then slowed down abruptly as the frequency increased. Therefore,

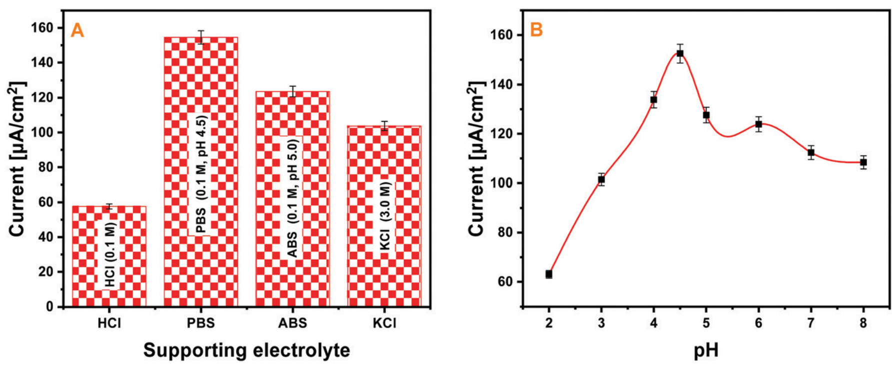

Fig. 10 Evaluation of (A) supporting electrolyte and (B) solution pH effects on SWV responses of 50 μM carbaryl at Pd/ZnO/APC/GCE.

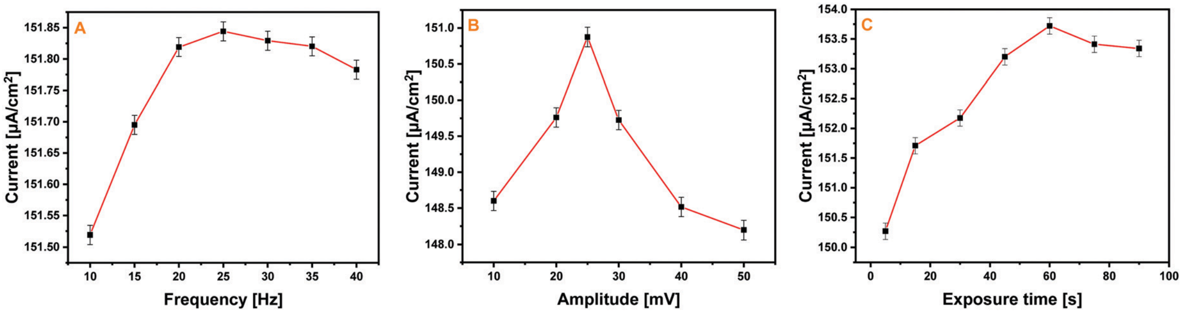

Fig. 11 Parameter optimization of SWV: (A) frequency, (B) amplitude, and (C) exposure times at the Pd/ZnO/APC/GCE in 0.1 M PBS (pH 4.5), containing 50 µM carbaryl.

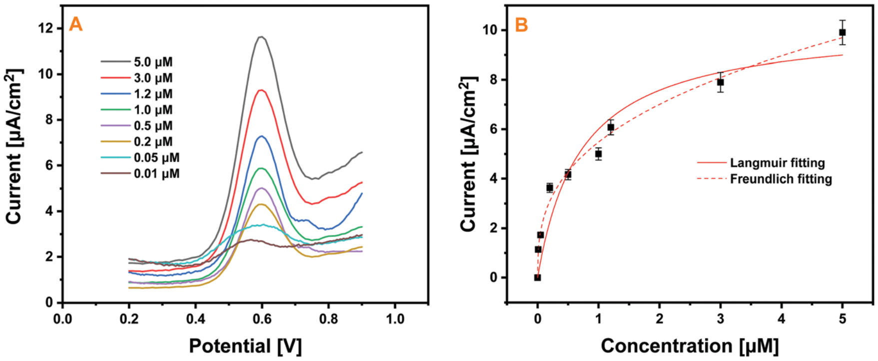

Fig. 12 (A) SWV sensorgrams of carbaryl oxidation with different concentrations 0.01, 0.05, 0.2, 0.5, 1.0, 1.2, 3.0, and 5.0 µM at Pd/ZnO/APC/GCE in 0.1 M PBS (pH 4.5) and (B) plots of peak currents *vs.* carbaryl concentrations fitted to the Langmuir and Freundlich models.

25 Hz was used as the suitable frequency for optimized amplitude that varied between 10 and 50 mV (Fig. 11B). The maximum current signal occurred at 25 mV, which was selected thereafter as the optimal square-wave amplitude for carbaryl detection. Finally, by fixing the amplitude at 25 mV and frequency at 25 Hz, the exposure time was assessed to be in a range from 5 to 90 s. The equilibrium and the threshold value of the current signal were reached within 60 s as seen in Fig. 11C. On this basis, a frequency of 25 Hz at 25 mV amplitude with over 60 s of exposure time was set to assess the SWV response toward carbaryl.

3.4.2. Calibration curves. To determine the analytical range of the developed sensor, the SWV response of the Pd/ZnO/APC/GCE was monitored by spiking various concentrations of carbaryl in the range of 5 to 0.01 µM in 0.1 M PBS (pH 4.5) under the optimum parameters described above. Fig. 12 displays the sensorgrams for the quantitative analysis of carbaryl oxidation current within the range between 0.2 and 0.9 mV and the corresponding calibration plot. As shown in Fig. 12A, well-defined oxidation peaks were observed, which tended to decline gradually with a decrease in the carbaryl concentration from 5 to 0.01 µM until there was no response recorded beyond the concentration of 0.01 µM. The limit of detection was determined experimentally as 0.01 µM, which was beyond the maximum acceptable concentration (MAC) established by the Food and Agriculture Organization (FAO) and the World Health Organization (WHO) (0.4 µM).[73] More detailed information on the Pd/ZnO/APC/GCE affinity towards carbaryl molecules can be learned by plotting the current intensity against the concentration of the target analyte as demonstrated in Fig. 12B. For that, two simulation adsorption models, namely Langmuir and Freundlich models were applied. The Langmuir model assumes an energetically equivalent distribution of active binding sites within the sorbent (homogenous), Where each active site is likely to interact with only one analyte molecule,[74] whereas Freundlich assumes the presence of heterogeneous surfaces with different affinities that allow multilayer adsorption by introducing the parameter m, *i.e.*, index of heterogeneity of the sorbent, into the binding affinity calculations. The parameter m varies in the range between 0 and 1; if m reaches 1, the heterogeneity of the system decreases, and the homogenous system is realized for $m = 1$.[75] Parameters extracted by fitting the experimental data using nonlinear regression are listed in Table 2. Either Langmuir or Freundlich can fit the data, but the Freundlich model appeared to be more adequate with a strong correlation coefficient value of

Table 2 Langmuir and Freundlich parameters

Fitting parameters	Langmuir	Freundlich
K_d (µM)	0.7110	0.1824
m		0.3549
R^2	0.9262	0.9915

Table 3 Comparison of performances of the present sensor with reported studies

Technique	Material	Linear range (μM)	LOD (μM)	Ref.
DPV	CoO/rGO/GCE	0.5 200	0.037	78
DPV	rGO/Cu/CuO Ag/GCE	0.05 20	0.005	24
DPV	LSXZ/CPE	1 100	0.30	70
SWV	GO IL/GCE	0.10 12.0	0.02	10
DPV	Poly *p*PDs IL/CPE	0.5 200	0.09	34
DPV	Carbon black NPs/SPE	0.1 100	0.048	79
Chronoamperometry	MWCNT/PANI/AChE/GCE	9.9 49.6	1.4	80
Chronoamperometry	AChE/cobalt phthalocyanine/CPE	50 750	4.0	81
SWV	BDD	2.5 30	0.04	82
SWV	Pd/ZnO/APC/GCE	0.01 5	0.01	Our work

CoO: cobalt oxide; rGO: reduced graphene oxide; CuO: copper oxide; LSXZ: low silica X zeolite; GO IL: graphene oxide ionic liquid; Poly pPDs IL: poly *p*Phenylenediamine ionic liquid; CPE: carbon paste electrode; SPE: screen printed electrode; MWCNT: multi walled carbon nanotube; PANI: polyaniline; BDD: boron doped diamond.

0.9915 and a high binding affinity (K_d) of 0.1824 μM. This satisfactory performance was achieved given the unique features of the Pd/ZnO/APC nanocomposite, such as the hierarchically porous framework, efficient absorptivity, and impressive electrocatalytic ability.

3.4.3. Comparative study. In comparative terms, the analytical performances of the developed sensor for the detection of carbaryl were matched with other relevant sensors already proposed in the literature. Table 3 lists the performances in terms of detection limit and linear dynamic range based on various electrochemical techniques and electrode materials. As can be seen, the detection limit and linear range of the Pd/ZnO/APC/GCE sensing were comparable with and even better than those obtained by the other modified electrodes, which made the developed sensor good enough to assess analytical activities. In addition, the actual intake of carbaryl was likely to be much lower than that achieved by conventional methods, such as spectrophotometry with a UV/VIS/NIR detector[76] or by HPLC with a UV/VIS detector, post-column[77] detection (detection limit 0.2 mg L^{-1} ≈ 1 μM). Therefore, this sensor could be utilized to analyze carbaryl residues in fresh water and food products to ensure healthy nutrition. Furthermore, it is worth noting that the proposed sensor is cheap and easy to fabricate.

3.4.4. Specificity, reproducibility, repeatability, and stability tests. To investigate the specificity of the developed sensor towards carbaryl, the effect of some commonly found interferents in real samples, such as electroactive inorganic (K^+, Na^+, Ca^{2+}, Mg^{2+}, NO^{3-}, and Cd^{2+}) and organic (acid ascorbic, atrazine, and bromoxynil) species, was determined by the fabricated sensor in 0.1 M PBS (pH 4.5) containing 1.0 μM carbaryl

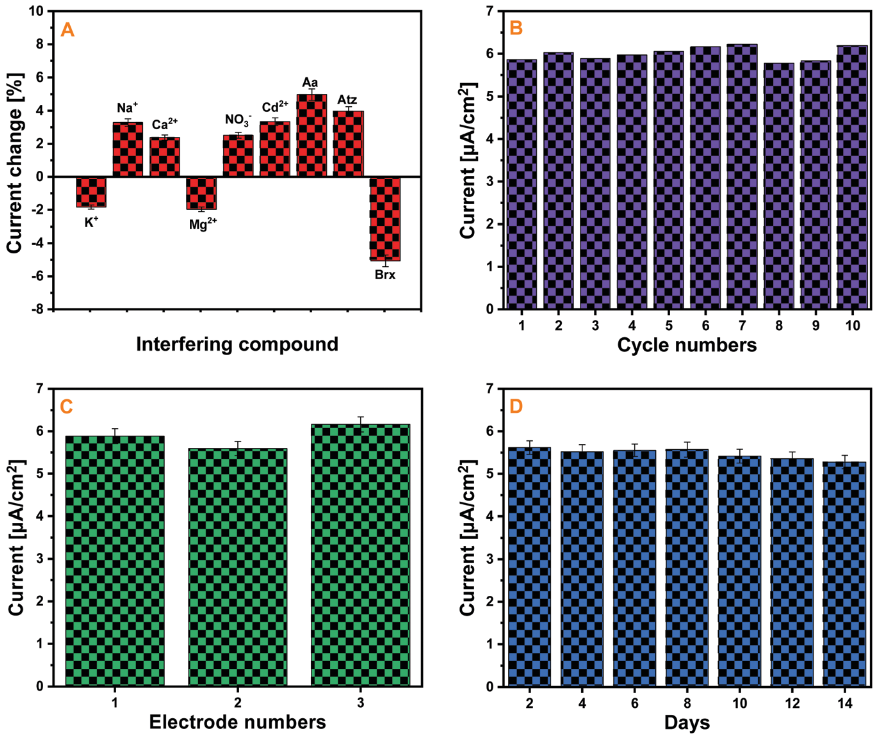

Fig. 13 (A) Interference, (B) reproducibility, (C) repeatability, and (D) stability measurements of the sensor.

under the same experimental conditions. The cross-reactivity of the sensor was measured in the presence of 20-folds of common metal ions and 10-folds of organic compounds; the degree of interference was expressed in terms of the relative standard deviation (RSD) of the blank solution (Fig. 13A). As reported in Fig. 13A, most of the interfering species exhibited a low degree of interference with standard deviation values below or near 5%, suggesting a negligible effect on the signal current for the optimized carbaryl sensing conditions. Commonly, an active substance is considered to be an interfering agent, when its influence on the peak current of the target analyte is above ±5%.[83] The results obtained here showed that the fabricated sensor had a strong anti-interference ability, which rendered it suitable for the detection of carbaryl pesticides in real samples.

The repeatability, reproducibility, and stability of the developed sensor were further evaluated in 0.1 M PBS (pH 4.5) containing 1.0 μM carbaryl under the established conditions; the goal was to test the sensor reliability for carbaryl detection. For repeatability (Fig. 13B), Pd/ZnO/APC/GCE was applied in 10 repetitive measurements toward the determination of (1.0 μM) carbaryl, and the relative standard deviation (RSD) of 10 such readings was 2.99%, indicating that our sensor possessed excellent repeatability. The electrode-to-electrode fabrication reproducibility was examined by three electrodes of the same batch (Fig. 13C). The results showed an average RSD of 3.35%, which indicates that the preparation method was highly reproducible and the constructed sensor had high precision. The storage stability of the sensor was checked by storing the Pd/ZnO/APC/GCE at room temperature for 15 days, and thereafter testing its sensitivity toward carbaryl every two days (Fig. 13D). About 93.31% of its initial sensitivity was retained, thus revealing operational stability. Nonetheless, the excellent repeatability, good reproducibility, and long-term stability make the proposed sensor reliable for practical use.

3.4.5. Realistic sample tests. To access the practical application of the developed sensor, the determination of carbaryl was carried out on real samples, including drinking water and tomato juice. Analytically, two different concentrations of carbaryl (0.4 and 1.0 μM) were spiked in drinking water and tomato juice samples, which were then analyzed using the proposed sensor under established conditions. Table 4 reports the data thus obtained. The recovery percentages were between 90% and 105% with RSD values between 4.2% and 5.1% ($n = 3$), which are satisfactory in terms of reliability and accuracy. Nevertheless, these results qualify the present sensor to monitor carbaryl residues in water bodies and complex food samples.

Table 4 Determination of carbaryl in drinking water and tomato juice samples

Sample	$[\text{Carbaryl}]_{\text{added}}$ (μM)	$[\text{Carbaryl}]_{\text{recovered}}$ (μM)	Recovery (%)	RSD (%)
Drinking water	1.0	1.05	105	4.33
	0.4	0.38	95	4.28
Tomato juice	1.0	0.94	94	4.81
	0.4	0.36	90	5.12

4. Conclusions

In summary, a new nanocomposite of Pd/ZnO/APC was obtained by carbonization of potato starch and wet-chemical method and confirmed by XRD, FT-IR, XPS, TEM, SEM, AFM, and N_2 adsorption/desorption measurements. The as-prepared nanocomposite was then employed as a bulk material to modify GCE and applied for the determination of carbaryl pesticide. The electrocatalytic properties of the modified electrode were studied by CV and the charge-transfer resistance was measured by the EIS technique; both parameters showed excellent electrocatalytic activity and favorable mass electron transfer, respectively, making the determination of carbaryl possible. Subsequently, the proposed sensor has been assessed over a low concentration range of carbaryl (5.0–0.01 μM). The calibration curve of this sensor revealed a low limit of detection (0.01 μM) and presented excellent repeatability, good reproducibility, and long-term stability of the material. Organic species and common inorganic ions showed negligible interference with the selective determination of the target analyte. Based on these characteristics, the established sensor was applied for the determination of carbaryl in drinking water and food samples, and the results are satisfactory. Therefore, the device usage can be expanded to other groups of pollutants to ensure better and real-time monitoring of water bodies and food safety.

Author contributions

Rihem Jemai: methodology and preparation, formal analysis, visualization. Mohamed Amine Djebbi: investigation, data curation, supervision, writing, editing. Navid Hussain: investigation, SEM and AFM analysis, review. Bingquan Yang: investigation, SEM and AFM analysis, review. Michael Hirtz: investigation, SEM and AFM analysis, review. Vanessa Trouillet: investigation, XPS analysis, review. Hafsia Ben Rhaiem: supervision, validation, funding acquisition. Abdesslem Ben Haj Amara: supervision, validation, funding acquisition.

Conflicts of interest

The authors declare that they have no known competing financial interests or personal relationships that could have influenced the work reported in this paper.

Acknowledgements

The authors would like to acknowledge all those who contributed their time and resources to the development of this work. This work was partly carried out with the support of the Karlsruhe Nano Micro Facility (KNMFi, **www.knmf.kit.edu**).

References

1 C.-P. Li, S. Fan, C. Yin, N. Zhang, S. Du and H. Zhao, *Anal. Methods*, 2014, **6**, 1914–1921.

2 Y. İpek, H. Dinçer and A. Koca, *J. Electrochem. Soc.*, 2014, **161**, B183–B190.
3 V. N. Mehta, N. Ghinaiya, J. V. Rohit, R. K. Singhal, H. Basu and S. K. Kailasa, *TrAC, Trends Anal. Chem.*, 2022, **153**, 116607.
4 A. Yaqub, S. R. Gilani, S. Bilal, A. Hayat, A. Asif and S. A. Siddique, *ACS Omega*, 2022, **7**, 149–159.
5 M. K. L. da Silva, H. C. Vanzela, L. M. Defavari and I. Cesarino, *Sens. Actuators, B*, 2018, **277**, 555–561.
6 T. Ung Thi Dieu and L. Nguyen Quang, *Adv. Nat. Sci.: Nanosci. Nanotechnol.*, 2020, **11**, 015010.
7 A. Sharma, V. Kumar, B. Shahzad, M. Tanveer, G. P. S. Sidhu, N. Handa, S. K. Kohli, P. Yadav, A. S. Bali, R. D. Parihar, O. I. Dar, K. Singh, S. Jasrotia, P. Bakshi, M. Ramakrishnan, S. Kumar, R. Bhardwaj and A. K. Thukral, *SN Appl. Sci.*, 2019, **1**, 1446.
8 C. Gupta Ramesh, *Toxicology of organophosphate and carbamate compounds*, Academic Press, Oxford, 2005.
9 T. Dong, J. Sun, B. Liu, Y. Zhang, Y. Song and S. Wang, *J. Sci. Food Agric.*, 2010, **90**, 1106–1112.
10 B. Liu, B. Xiao and L. Cui, *J. Food Compos. Anal.*, 2015, **40**, 14–18.
11 M.-L. Chin-Chen, M. Rambla-Alegre, A. Durgbanshi, D. Bose, S. K. Mourya, J. Esteve-Romero and S. Carda-Broch, *Int. J. Anal. Chem.*, 2012, **2012**, 1–7.
12 C. Raeppel, M. Nief, M. Fabritius, L. Racault, B. M. Appenzeller and M. Millet, *J. Chromatogr. A*, 2011, **1218**, 8123–8129.
13 E. K. Fodjo, S. Riaz, D.-W. Li, L.-L. Qu, N. P. Marius, T. Albert and Y.-T. Long, *Anal. Methods*, 2012, **4**, 3785.
14 F. K. Alsammarraie and M. Lin, *J. Agric. Food Chem.*, 2017, **65**, 666–674.
15 D. K. Sharma, T. Dharmani and N. Sharma, *Bull. Chem. Soc. Ethiop.*, 2015, **29**, 173.
16 Z. Long, S. Shen, Y. Lu, W. Lan, J. Chen and H. Qiu, *Anal. Bioanal. Chem.*, 2019, **411**, 4221–4229.
17 G. Z. Tsogas, D. L. Giokas, P. G. Nikolakopoulos, A. G. Vlessidis and N. P. Evmiridis, *Anal. Chim. Acta*, 2006, **573–574**, 354–359.
18 M. P. García de Llasera and M. Bernal-González, *Water Res.*, 2001, **35**, 1933–1940.
19 A. Y. Boroduleva, J. Wu, Q. Yang, H. Li, Q. Zhang, P. Li and S. A. Eremin, *Anal. Methods*, 2017, **9**, 6814–6822.
20 C. Zhang, H. Cui, Y. Han, F. Yu and X. Shi, *Food Chem.*, 2018, **240**, 893–897.
21 D. J. Joshi, J. R. Koduru, N. I. Malek, C. M. Hussain and S. K. Kailasa, *TrAC, Trends Anal. Chem.*, 2021, **144**, 116448.
22 L. Zhao, F. Zhao and B. Zeng, *Int. J. Electrochem.*, 2014, **9**, 1366–1377.
23 T. Rahmani, H. Bagheri, M. Behbahani, A. Hajian and A. Afkhami, *Food Anal. Methods*, 2018, **11**, 3005–3014.
24 P. Hashemi, N. Karimian, H. Khoshsafar, F. Arduini, M. Mesri, A. Afkhami and H. Bagheri, *Mater. Sci. Eng., C*, 2019, **102**, 764–772.
25 H. Lü, L. Yang, Y. Zhou, R. Qu, Y. Xu, S. Shang and N. Hui, *J. Electrochem. Soc.*, 2021, **168**, 047506.
26 C. S. Fang, K. H. Oh, J. K. Park and H. Yang, *Electroanalysis*, 2017, **29**, 339–344.
27 A. Pop, F. Manea, A. Flueras and J. Schoonman, *Sensors*, 2017, **17**, 2033.
28 T. Liu, H. Su, X. Qu, P. Ju, L. Cui and S. Ai, *Sens. Actuators, B*, 2011, **160**, 1255–1261.
29 I. Cesarino, F. C. Moraes and S. A. S. Machado, *Electroanalysis*, 2011, **23**, 2586–2593.
30 A. Hatefi-Mehrjardi, *Electrochim. Acta*, 2013, **114**, 394–402.
31 C. S. Santos, R. Mossanha and C. A. Pessôa, *J. Appl. Electrochem.*, 2015, **45**, 325–334.
32 L. F. Loguercio, A. Thesing, P. Demingos, C. D. L. de Albuquerque, R. S. B. Rodrigues, A. G. Brolo and J. F. L. Santos, *Sens. Actuators, B*, 2021, **339**, 129875.
33 E. V. Dorozhko, A. S. Gashevskay, E. I. Korotkova, J. Barek, V. Vyskocil, S. A. Eremin, E. V. Galunin and M. Saqib, *Talanta*, 2021, **228**, 122174.
34 F. E. Salih, L. Oularbi, E. Halim, M. Elbasri, A. Ouarzane and M. El Rhazi, *Electroanalysis*, 2018, **30**, 1855–1864.
35 F. C. Moraes, L. H. Mascaro, S. A. S. Machado and C. M. A. Brett, *Talanta*, 2009, **79**, 1406–1411.
36 W. Chen, Y. Liu, Y. Zhang, J. Fang, P. Xu, J. Xu, X. Li, C.-C. Liu and W. Wen, *J. Mater. Chem. A*, 2017, **5**, 7064–7071.
37 L. Redivo, M. Stredanský, E. De Angelis, L. Navarini, M. Resmini and Ĺ. Švorc, *R. Soc. Open Sci.*, 2018, **5**, 172146.
38 M. Hassler, *Coatings for Biomedical Applications*, Elsevier, 2012, pp. 75–105.
39 J. Liu, C. Guo, C. M. Li, Y. Li, Q. Chi, X. Huang, L. Liao and T. Yu, *Electrochem. Commun.*, 2009, **11**, 202–205.
40 T. Yumak, F. Kuralay, M. Muti, A. Sinag, A. Erdem and S. Abaci, *Colloids Surf., B*, 2011, **86**, 397–403.
41 B. Saptaka, M. Bidyarani, K. B. Chandra, A. Tanvi Agarkar and K. Sanjeev, *IEEE Sens. J.*, 2021, **21**, 14601–14608.
42 R. A. Dar, G. A. Naikoo, A. K. Srivastava, I. U. Hassan, S. P. Karna, L. Giri, A. M. H. Shaikh, M. Rezakazemi and W. Ahmed, *Sci. Rep.*, 2022, **12**, 117.
43 E. Salih, M. Mekawy, R. Y. A. Hassan and I. M. El-Sherbiny, *J. Nanostruct. Chem.*, 2016, **6**, 137–144.
44 E. H. Umukoro, M. G. Peleyeju, A. O. Idris, J. C. Ngila, N. Mabuba, L. Rhyman, P. Ramasami and O. A. Arotiba, *RSC Adv.*, 2018, **8**, 10255–10266.
45 A. A. Ismail, F. A. Harraz, M. Faisal, A. M. El-Toni, A. Al-Hajry and M. S. Al-Assiri, *Superlattices Microstruct.*, 2016, **95**, 128–139.
46 R. Miao, B. Tao, F. Miao, J. Zhang and P. K. Chu, *J. Photochem. Photobiol., A*, 2020, **401**, 112785.
47 R. Madhu, V. Veeramani, S.-M. Chen, P. Veerakumar, S.-B. Liu and N. Miyamoto, *Phys. Chem. Chem. Phys.*, 2016, **18**, 16466–16475.
48 T. Zhang, H. Jin, Y. Fang, J. Guan, S. Ma, Y. Pan, M. Zhang, H. Zhu, X. Liu and M. Du, *Mater. Chem. Phys.*, 2019, **225**, 433–442.
49 X. Zhu, B. Liu, S. Chen, L. Wu, J. Yang, S. Liang, K. Xiao, J. Hu and H. Hou, *J. Electrochem. Soc.*, 2020, **167**, 087505.
50 M. A. Djebbi, L. Allagui, M. S. El Ayachi, S. Boubakri, N. Jaffrezic-Renault, P. Namour and A. Ben Haj Amara, *ACS Appl. Nano Mater.*, 2022, **5**, 546–558.
51 Y. Song, Y. Chen, J. Wu, Y. Fu, R. Zhou, S. Chen and L. Wang, *J. Alloys Compd.*, 2017, **694**, 1246–1253.

52 W. Dong, L. Zhang, C. Wang, C. Feng, N. Shang, S. Gao and C. Wang, *RSC Adv.*, 2016, **6**, 37118–37123.

53 Y. Hu, K. Xie, H. Wang, C. Yuan, B. Cao, L. Qian, S. Wang, F. Fazeli Zafar, K. Ding and Q. Wang, *J. Anal. Appl. Pyrolysis*, 2021, **157**, 105221.

54 H. Salmanvandi, P. Rezaei and Y. Tamsilian, *ACS Omega*, 2020, **5**, 13176–13184.

55 X. Han, L. Sun, F. Wang and D. Sun, *J. Mater. Chem. A*, 2018, **6**, 18891–18897.

56 A. G. Marrani, F. Caprioli, A. Boccia, R. Zanoni and F. Decker, *J. Solid State Electrochem.*, 2014, **18**, 505–513.

57 P. Veerakumar, V. Veeramani, S.-M. Chen, R. Madhu and S.-B. Liu, *ACS Appl. Mater. Interfaces*, 2016, **8**, 1319–1326.

58 J. Zhang, H. Zhang, J. Wu and J. Zhang, *Pem Fuel Cell Testing and Diagnosis*, 2013, pp. 283–335.

59 K. Dujearic-Stephane, M. Gupta, A. Kumar, V. Sharma, S. Pandit, P. Bocchetta and Y. Kumar, *J. Compos. Sci.*, 2021, **5**, 66.

60 M. A. Djebbi, S. Boubakri, M. Braiek, N. Jaffrezic-Renault, P. Namour and A. B. H. Amara, *Electroanalysis*, 2020, **32**, 1186–1197.

61 L. Y. Yan, U. Binesh and M. C. Shen, *Int. J. Electrochem. Sci.*, 2011, **6**, 3902.

62 M. A. Djebbi, S. Boubakri, M. Braiek, N. Jaffrezic-Renault, P. Namour and A. B. H. Amara, *Electrochem. Sci. Adv.*, 2021, **1**, e2000019.

63 M. A. Djebbi, S. Boubakri, M. Braiek, N. Jaffrezic-Renault, P. Namour and A. Ben Haj Amara, *J. Electrochem. Soc.*, 2021, **168**, 057529.

64 R. Miao, B. Tao, F. Miao, J. Zhang and P. K. Chu, *J. Photochem. Photobiol., A*, 2020, **401**, 112785.

65 E. H. Umukoro, M. G. Peleyeju, A. O. Idris, J. C. Ngila, N. Mabuba, L. Rhyman, P. Ramasami and O. A. Arotiba, *RSC Adv.*, 2018, **8**, 10255–10266.

66 H. T. Purushothama, Y. A. Nayaka, M. M. Vinay, P. Manjunatha, R. O. Yathisha and K. V. Basavarajappa, *J. Sci.: Adv. Mater. Devices*, 2018, **3**, 161–166.

67 B. Mutharani, P. Ranganathan and S.-M. Chen, *J. Taiwan Inst. Chem. Eng.*, 2019, **96**, 599–609.

68 E. Laviron, *J. Electroanal. Chem. Interfacial Electrochem.*, 1974, **52**, 355–393.

69 H. Wei, J.-J. Sun, Y.-M. Wang, X. Li and G.-N. Chen, *Analyst*, 2008, **133**, 1619.

70 F. E. Salih, B. Achiou, M. Ouammou, J. Bennazha, A. Ouarzane, S. A. Younssi and M. El Rhazi, *J. Adv. Res.*, 2017, **8**, 669–676.

71 Y. Ni, L. Wang and S. Kokot, *Anal. Chim. Acta*, 2001, **439**, 159–168.

72 B. Kaur and R. Srivastava, *Electroanalysis*, 2014, **26**, 1739–1750.

73 FAO/WHO, Evaluations of some pesticide residues in food, WHO Pesticide Residue Series, (3), World Health Organization, Geneva, 1974.

74 L. Irving, *J. Am. Chem. Soc.*, 1918, **40**, 1361–1403.

75 F. Herbert, Over the adsorption in solution, *J. Phys. Chem.*, 1906, **57**, 385–471.

76 L. Alvarez-Rodríguez, Ll Monferrer-Pons, J. S. Esteve-Romero, M. C. García-Alvarez-Coque and G. Ramis-Ramos, *Analyst*, 1997, **122**, 459–463.

77 D. C. Portela, I. M. F. Pereira, P. Paiga, C. Delerue-Matos and M. C. V. F. Vaz, *Anal. Bioanal. Chem.*, 2003, **377**, 356–361.

78 M. Wang, J. Huang, M. Wang, D. Zhang and J. Chen, *Food Chem.*, 2014, **151**, 191–197.

79 F. Della Pelle, C. Angelini, M. Sergi, M. Del Carlo, A. Pepe and D. Compagnone, *Talanta*, 2018, **186**, 389–396.

80 I. Cesarino, F. C. Moraes, M. R. V. Lanza and S. A. S. Machado, *Food Chem.*, 2012, **135**, 873–879.

81 J. Caetano and S. A. S. Machado, *Sens. Actuators, B*, 2008, **129**, 40–46.

82 L. Codognoto, S. T. Tanimoto, V. A. Pedrosa, H. B. Suffredini, S. A. S. Machado and L. A. Avaca, *Electroanalysis*, 2006, **18**, 253–258.

83 W. Zhang, H. Zhang, S. E. Williams and A. Zhou, *Talanta*, 2015, **132**, 321–326.